Materials & Design 216 (2022) 110516

Contents lists available at ScienceDirect

Materials & Design

journal homepage: www.elsevier.com/locate/matdes

Controlling the Young's modulus of a ß-type Ti-Nb alloy via strong texturing by LPBF

Stefan Pilz [a,*], Tobias Gustmann [a], Fabian Günther [b,c], Martina Zimmermann [b,c], Uta Kühn [a], Annett Gebert [a]

[a] Institut of Complex Materials, Leibniz IFW Dresden, Helmholtzstr. 20, 01069 Dresden, Germany
[b] Institute of Materials Science, TU Dresden, Helmholtzstr. 7, 01069 Dresden, Germany
[c] Fraunhofer Institute for Material and Beam Technology (Fraunhofer IWS), Winterbergstr. 28, 01277 Dresden, Germany

HIGHLIGHTS

- The ß-type Ti-42Nb alloy was processed by laser powder bed fusion (LPBF) with an infrared top hat laser configuration.
- A high build rate of 12.5 mm^3/h, as well as a high relative density of 99.96% was achieved.
- The unique microstructure created by the top hat laser results in a strong elastic anisotropy.
- The Young's modulus along the built direction was reduced by 30% compared to the Gaussian reference samples.

GRAPHICAL ABSTRACT

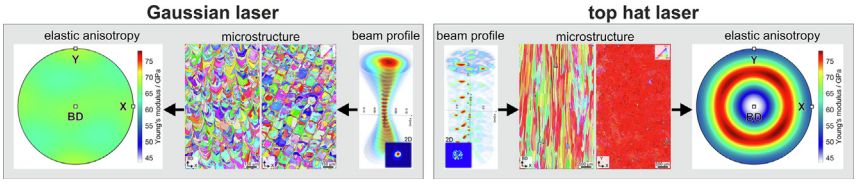

ARTICLE INFO

Article history:
Received 13 January 2022
Revised 23 February 2022
Accepted 3 March 2022
Available online 07 March 2022

Keywords:
Beta Titanium alloy
Mechanical anisotropy
Texture
Laser powder bed fusion (LPBF)
Top Hat Laser

ABSTRACT

The ß-type Ti-42Nb alloy was processed by laser powder bed fusion (LPBF) with an infrared top hat laser configuration aiming to control the Young's modulus by creating an adapted crystallographic texture. Utilizing a top hat laser, a microstructure with a strong ⟨0 0 1⟩ texture parallel to the building direction and highly elongated grains was generated. This microstructure results in a strong anisotropy of the Young's modulus that was modeled based on the single crystal elastic tensor and the experimental texture data. Tensile tests along selected loading directions were conducted to study the mechanical anisotropy and showed a good correlation with the modeled data. A Young's modulus as low as 44 GPa was measured parallel to the building direction, which corresponds to a significant reduction of over 30% compared to the Young's modulus of the Gaussian reference samples (67–69 GPa). At the same time a high 0.2% yield strength of 674 MPa was retained. The results reveal the high potential of LPBF processing utilizing a top hat laser configuration to fabricate patient-specific implants with an adapted low Young's modulus along the main loading direction and a tailored mechanical biofunctionality.

1. Introduction

Due to its high strength and corrosion resistance, the α+ß-type Ti-6Al-4V alloy has been used as load-bearing implant material for orthopedic and trauma applications in recent decades [1]. However, because of its critical alloying elements V and Al, more and more concerns regarding allergic reactions and cytotoxicity arise [2]. Furthermore, the large mismatch between its high Young's modulus (120 GPa) and that of cortical bone (10–30 GPa) leads to the so called "stress shielding" effect, which complicates bone healing processes [3]. A large stiffness difference

* Corresponding author.
E-mail address: s.pilz@ifw-dresden.de (S. Pilz).

https://doi.org/10.1016/j.matdes.2022.110516
0264-1275/

between implant and adjacent bone tissue causes an uneven stress distribution. The load is mainly transferred to the much stiffer implant, whereby the bone is shielded. Thus, a mechanical stimulation of bone tissue regeneration is suppressed. To overcome these issues, intense research was done to develop novel ß-type Ti alloys with biocompatible alloying elements and low Young's modulus values. Most of these novel alloys are based on the Ti-Nb system. Compared to Ti-6Al-4V, these alloys have an increased density caused by their relatively high Nb content [4], but exhibit significantly decreased Young's modulus values in the range of 50–65 GPa in the cast and solution treated state [5]. Thermomechanical processing is done to control the microstructure and to adjust suitable strength and fatigue resistance values [5–7]. Furthermore, the strong passivation ability of β-type Ti-Nb alloys in bio-fluids yields a superior corrosion behaviour and very low metal release rates which, in consequence, was found to support bone cell activity [8–10].

Meanwhile, laser powder bed fusion (LPBF), also known as selective laser melting (SLM), has attracted increasing interest in research and selected technology branches, viz. medical engineering and part production, due to its ability to fabricate patient specific implants as well as to realize new implant designs that are hard to fabricate or even not feasible with conventional manufacturing technologies [11]. Most of the past and recent research activities regarding LPBF of Ti-based alloys are focused on α-type (cp-Ti) and α+ß-type (Ti-6Al-4V, Ti-6Al-7Nb) materials, which have found their way to commercial implant production. Only limited numbers of published studies are available so far regarding LPBF of near-ß and ß-type alloys [12–14]. In the field of ß-type Ti-Nb-based alloys for biomedical applications Ti-Nb [15–23], Ti-Nb-Zr [24–33], Ti-Nb-Ta-Zr [34,35], and Ti-Nb-Zr-Sn [36–40] alloys have been reported to be processed by LPBF. Due to the high cooling rates that arise during LPBF processing [41], obtained ß-type Ti-Nb alloy specimens exhibit unique microstructures and therefore, offer superior mechanical properties, when compared to cast and solution treated counterparts. Furthermore, LPBF offers the opportunity to control the local microstructure and texture and therefore, the local mechanical properties of parts by applying different processing parameters, such as the scanning speed and laser power or via using adjusted exposure strategies (e.g., applied scanning pattern, vector rotation per layer) [42–45]. This approach enables the fabrication of implants (e.g., hip stems) that can be locally adapted to the applied mechanical load and to the high elastic anisotropy of human bone [46,47].

An important, but not often recognized feature that defines the microstructure of LPBF-processed specimens is the size and the profile of the applied laser beam. It can strongly affect the melt pool geometry and the solidification conditions. Most of the available industrial LPBF systems are equipped with an infrared laser with a near Gaussian intensity distribution and a beam diameter smaller than 100 μm [48]. These 'small spot' configurations have two main limitations: (1) vapor-induced instabilities with subsequent ejection of spatters and (2) the increase of the build-up rate is limited due to process instabilities [48]. To overcome these issues, high-power laser sources (around 1000 W) with an increased spot size and a top hat intensity distribution were introduced [48–50]. Montero-Sistiaga et al. [51,52] showed, that the build-up rate can be increased by around 2.5-fold for 316L and Hastelloy X when a laser with a 0.7 mm beam size and a top hat intensity distribution is used [41,42]. Furthermore, an increased process stability and a reduced spattering was observed by Sow et al. [48]. The effect of a significantly increased beam size and a top hat profile on the resulting microstructure was only studied for a limited number of alloys, namely Ni-based alloys [52–54], steels [51,55,56] and Al-based alloys [57,58]. In this context, a very strong ⟨0 0 1⟩ texture development parallel to the building direction in combination with epitaxial grain growth is reported by some authors [53–55]. With respect to Ti-based alloys, only one study by Huang et al. [23] is available, demonstrating the beneficial influence of a top hat laser configuration on the Nb inclusion content of in-situ alloyed Ti-34Nb. Although the influence of a top hat laser configuration on pre-alloyed Ti-Nb powder remains unclear, they also reported a strong ⟨0 0 1⟩ texture development and epitaxial grain growth along the building direction. Unfortunately, the mechanical properties of the samples were not investigated along the building direction. A strong ⟨0 0 1⟩ texture could be beneficially in lowering the Young's modulus, as ß-type Ti alloy single crystals show a clear orientation dependence of the Young's modulus. Thereby, the highest Young's modulus value exists along the ⟨1 1 1⟩ directions and the lowest along the ⟨0 0 1⟩ directions [42,59–62]. Therefore, the use of single crystals as bone implant materials with a ⟨0 0 1⟩ crystal direction parallel to the loading direction was proposed to reduce the stress shielding effect [59–61,63]. However, until now new processes to fabricate large single crystals are not established and would be very cost intensive. Therefore, their practical implementation is not expectable.

With the present work, we propose the use of a high-power top hat laser with an increased beam size to produce load-bearing bulk implants with a strong ⟨0 0 1⟩ texture from ß-type Ti-Nb powders. Such a highly textured ß-type microstructure can help to control the Young's modulus of as-built specimen relative to the building direction. In perspective, those anisotropic implants with their lowest stiffness direction oriented in the main loading direction could significantly reduce stress shielding. In addition, by utilizing a high-power top hat laser during LPBF processing of Ti-Nb alloys, build-up rates can be significantly enhanced (increased hatching distance and layer thickness) which reduces costs and development times of possible implant prototypes with adjusted properties.

In order to verify this approach, a novel ß-type Ti-42Nb alloy is comparatively processed by LPBF with a Gaussian laser (small beam diameter) and a top hat laser (increased beam diameter). The microstructure and the texture after processing are characterized in-depth and the mechanical properties are determined parallel, perpendicular and at an angle of 45° with respect to the building direction via tensile testing.

2. Materials and methods

2.1. Materials

Pre-alloyed, gas-atomized Ti-42Nb (wt.%) powder (AMtrinsic® Spherical Ti-42Nb [64]) was supplied by TANIOBIS GmbH (Goslar, Germany). The powder particle size range was 10–63 μm. The chemical composition of the powder was determined by inductively coupled plasma optical emission spectrometry (ICP-OES) as Ti = 57.9 ± 0.33 wt% and Nb = 41.49 ± 0.25 wt%. The oxygen content was analyzed by carrier gas hot extraction (LECO TC-436DR) as 0.285 ± 0.001 wt%. The experimentally determined chemical composition corresponds well with the nominal one.

2.2. LPBF fabrication

A SLM280 Generation 2.0 dual laser machine (SLM Solutions Group AG, Germany) was employed to fabricate cuboids with a dimension of 9 mm × 19 mm × 40 mm. Two different infrared laser sources were used: (1) a laser with a Gaussian intensity distribution (700 W maximum laser power) and a minimum beam size of approx. 80 μm as well as (2) a laser with a top hat intensity distribution (1000 W maximum laser power) and a constant beam size of approx. 680 μm. The power output (Coherent Laser Power

Energy Meter, Coherent, USA) and beam profiles (Cinogy Focus Beam Profiler FBP-0018, Cinogy, Germany) have been validated during a machine checkup. The deviation of the applied laser power with respect to the measured values is around 20 W and, thus, negligible for our study. The beam profiles were captured applying 15 to 70% (Gaussian) as well as 10% (top hat) of the available maximum laser power. A build envelope of 100 mm × 100 mm (180 mm maximum height) was used, while the substrate plates were heated and held constant at 80 °C prior to processing. Process parameters, viz. laser power, scanning speed and hatching distance, were optimized in a preliminary study to fabricate samples with a high relative density (>99%). The layer thickness was adjusted to 100 μm. An overview of the applied process parameters is given in Table 1. For the manufactured cuboids, the z-axis was defined to be parallel to the building direction (see Fig. 1(c)).

2.3. Characterization

Specimens for microstructural investigations were mechanically ground using SiC paper (P400–P2500). For the final polishing step, a mixture of colloidal SiO_2 (90 vol%) and H_2O_2 (10 vol%) was used. The relative density of the samples was evaluated on polished cross sections utilizing a digital microscope (VHX7000, Keyence Deutschland GmbH, Germany). Scanning electron microscope (SEM) imaging and electron backscatter diffraction (EBSD) analysis were carried out using a Leo Gemini 1530 (Zeiss AG, Germany) equipped with a e-Flash^{HR} EBSD system (Bruker GmbH, Germany). For the evaluation of EBSD measurements and the texture analysis, the open-source toolbox MTEX (v.5.6, https://mtex-toolbox.github.io) [37] was used. A minimum grain boundary threshold of 15° was chosen for grain detection. To evaluate the influence of the crystallographic texture on the Young's modulus, the orientation dependence of the elastic properties of the material was calculated based on the determined texture data with the Hill approximation [65,66].

X-ray diffraction (XRD) analysis was performed on mechanically thinned disks (thickness = 80 μm) using a STOE Stadi P diffractometer (STOE & Cie GmbH, Germany) in transmission mode using Mo $K_{\alpha 1}$ radiation (λ = 0.7093187 Å).

To study the influence of the different laser sources on the mechanical properties, flat bar tensile samples with a gauge length of 5.5 mm, a width of 1 mm and a thickness of 0.85 mm were machined by electro discharge machining (EDM) from LPBF cuboids (see Fig. 1(c) and (d)). The samples were extracted parallel, perpendicular and with an angle of 45° with respect to the building direction (BD). Uniaxial tensile tests were carried out using a tensile-compression module (Kammrath & Weiss GmbH, Germany) with a 5 kN load cell and an extension rate of 0.00175 mm/s. For strain measurement a microDAC (Chemnitzer Werkstoffmechanik GmbH, Germany) video extensometer was applied and the Young's modulus was calculated from the slope of the stress–strain curves. For each sample state, at least three samples were tested.

3. Results and discussion

3.1. Microstructure characterization

After LPBF processing, the density of both Ti-42Nb sample states was determined via optical microscopy using three different cross-sectional planes (X-BD, Y-BD and X-Y). For samples processed with the Gaussian laser, a relative density of 99.94 ± 0.00 8% was determined. The density of the top hat laser samples was slightly higher and found to be at 99.96 ± 0.011%. During processing, almost no splats were ejected when the top hat laser was employed. This indicates that evaporation effects were avoided (conduction welding) and a more stable process was present. Therefore, porosity formation was reduced to an absolute minimum [48].

Due to the relative high solidification and cooling rates that arise during LPBF processing, a pure ß-type microstructure (bcc), without any additional phases, is detected by XRD analysis irrespective of the laser source applied (Fig. 2).

The SEM images of the X-BD cross sections in Fig. 3(a) and (b) show clear differences in the melt pool morphology for the applied laser sources (SEM images of the X-Y cross sections are shown in Supplementary Fig. 1). For the Gaussian laser, the melt pool shows a more hemispherical shape with a melt pool depth of around 275 μm and a width bigger than 100 μm. The top hat laser (Fig. 3 (b)) produces a nearly identical penetration depth of around 250 μm, but the melt pool is nearly planar with a significantly larger width (above 800 μm). The depth-over-width ratio is below 0.31 which confirms that the top hat laser, irrespective of the high laser power applied, works in conduction mode due to the enhanced beam diameter. In comparison, the Gaussian laser operates in the keyhole mode yielding a depth-over-width ratio of around 2.75 [48,67].

The higher magnified images in Fig. 3(c) and (d) reveal a cellular/dendritic microstructure for both samples. This is a typical phenomenon for LPBF-processed Ti alloys (e.g., Ti-Nb, Ti-5Al-5V-5Mo-3Cr) [20,68]. Significant differences can be seen regarding the cell size. For the Gaussian samples, the cell size is in the range of up to 0.5 μm and varies strongly within the melt pool (intersects: equiaxed, center: elongated/epitaxial). In contrast, the top hat laser specimens show a nearly constant cell size of about 3–5 μm while the cells span over the whole melt pool. As the cell size is related to the applied cooling rate during solidification, a lower and more homogeneous cooling rate can therefore be concluded for the top hat laser sample. The cell orientation is also strongly influenced by the applied laser beam. Due to the complex heat flow, the cell orientation varies significantly within the former melt pool, for the Gaussian laser. For the top hat laser, the cells show a consistent growth direction parallel to the build direction. This implies a highly oriented and uniform heat flow towards the substrate plate [48].

To investigate the effect of the laser source on the grain morphology of the Ti-42Nb specimen, EBSD analyses were performed on cross sections parallel (X-Y) and perpendicular (X-BD) to the build plate. Inverse pole figure mappings superimposed with the

Table 1
Applied process parameters for the fabrication of Ti-42Nb LPBF specimens using a Gaussian and top hat laser source. In addition, the volume energy inputs, and build-up rates are listed. The layer thickness was held constant at 100 μm.

Infrared laser type	Laser power (W)	Scanning speed (mm/s)	Hatching distance (mm)	Energy Input (J/mm^3)	Build-up rate (mm^3/s)	Laser beam diameter (μm)
Gaussian laser	550	1100	0.15	33.33	16.5 (59.4 cm^3/h)	140
Top hat laser	950	250	0.5	76	12.5 (45.5 cm^3/h)	670

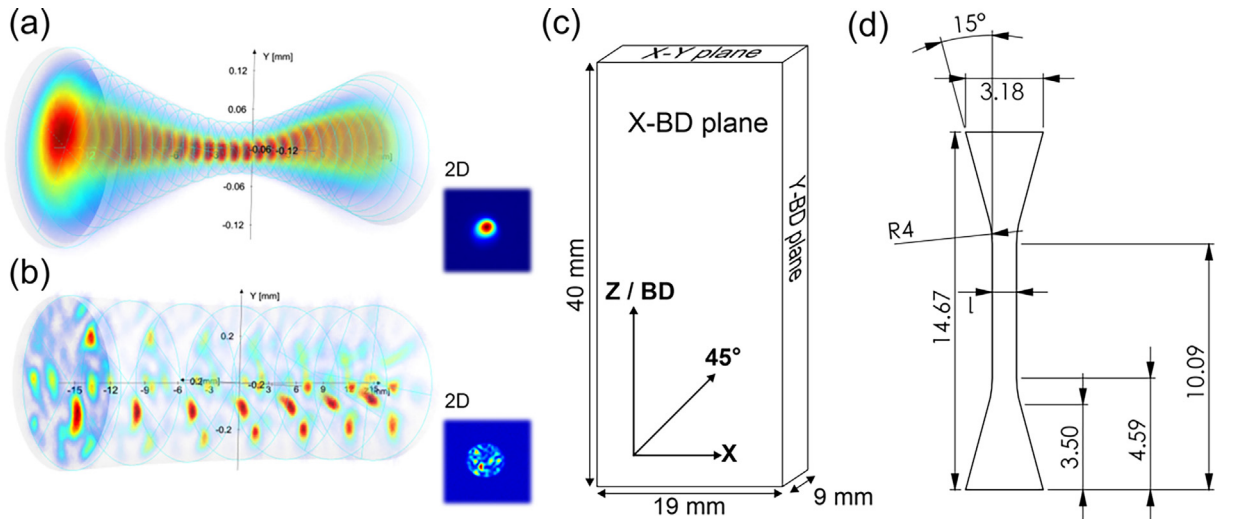

Fig. 1. Captured beam profile of the (a) Gaussian (at 490 W) and (b) top hat laser (at 100 W). The insets show the energy distribution as a 2D visualization. In contrast to the top hat laser (no beam waist), the Gaussian beam showed a pronounced shift of the observed waist from the zero position at higher laser powers (above 200 W). For working with the Gaussian beam and high laser powers, the focus position was shifted to 4 mm and thus, further defocused to avoid keyhole formation during processing. A relative weak and scattered energy distribution was observed for the top hat laser due to the relative low power applied. The profiles were recorded by SLM Solutions Group AG based on internal guidelines and found to be in the range of the required machine settings. In (c), the sample coordinate system of a fabricated Ti-42Nb cuboid is highlighted to illustrate the sample orientation which has been conducted in this study. The geometrical features of the used tensile test geometry (in mm) are presented in (d).

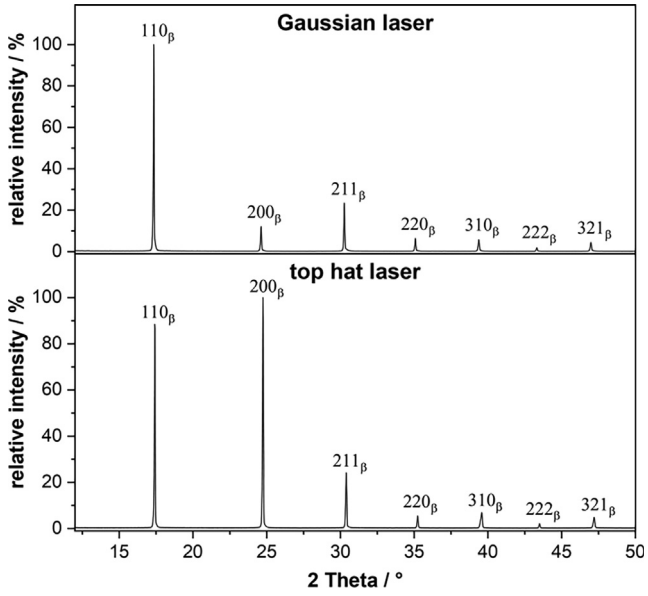

Fig. 2. XRD patterns of the Ti-42Nb alloy processed with a Gaussian and a top hat laser source.

calculated high angle boundaries (misorientation $\geq 15°$), in black, and low angle boundaries (misorientation $< 15°$), in grey, are highlighted in Fig. 4.

For the Gaussian laser (Fig. 4(a) and (b)), the grains have an irregular or V-shaped morphology in the X-BD cross section. The mean grain size (circular equivalent diameter) is around 175 μm. In the X-Y cross section the morphology of the grains is square shaped and the applied scan paths are apparent. Beside the change of the grain morphology and distribution, the grain size is in the same range (d = 160 μm). For both investigated sample planes, only a small number of low angle boundaries is present.

A completely different microstructure is obtained when the alloy is processed with the top hat laser. The grains and sub grains are elongated (several millimeters) along the building direction and have a high aspect ratio (Fig. 4(c)). This significant change of the grain morphology and grain size is related to the altered melt pool and solidification characteristics caused by the different laser types and processing parameters. As the heat flow and thereby the solidification direction varies strongly within the hemispherical melt pool of the Gaussian laser (Fig. 3(c)), an epitaxial growth of columnar grains is suppressed by the applied scan vector rotation [44,69,70]. For the top hat laser, the planar melt pool shape and the highly oriented heat flow towards the substrate favors epitaxial growth of columnar grains along BD, as the heat flow direction and the normal of the solid–liquid interface are nearly parallel [23,53,71]. In this case, the applied scanning rotation does not lead to a segmentation of columnar grains, because the heat flow and thus the solidification direction are mostly independent of the applied scanning direction. Furthermore, the lower melt pool velocity caused by the relatively low laser scanning speed (250 mm/s) and the significantly increased melt pool size, due to the large beam diameter, decreases the cooling rate and are the primary reasons for the grain coarsening observed for the top hat laser samples [23].

Due to the large dimensions as well as the pronounced aspect ratio of the grains, a description of the grain size by the circular equivalent diameter is not possible for this type of microstructure. Therefore, the grain boundary and sub grain boundary density (total boundary length per measurement area) values were calculated to compare both microstructures. For the Gaussian laser, the density of high angle boundaries in the X-BD and the X-Y cross section is 0.0375 μm^{-1} and 0.0432 μm^{-1}, respectively. This difference is in good accordance with the slight difference observed for the circular equivalent diameter. The density of low angle boundaries is one magnitude lower (0.0066 μm^{-1} and 0.0069 μm^{-1}, respectively) and is in the same range for both observation planes. In comparison, the density of high angle boundaries is significantly reduced by about one order of magnitude to 0.004 μm^{-1} (BD-X cross section) and 0.006 μm^{-1} (X-Y cross section) for the top hat laser samples. This implies a significantly increased grain size for these samples. Due to the columnar grain growth and the resulting high aspect ratio of the grains along BD, the high angle boundary density is about one-third higher for the X-Y cross section. Furthermore, the density of low angle boundaries is altered for the different

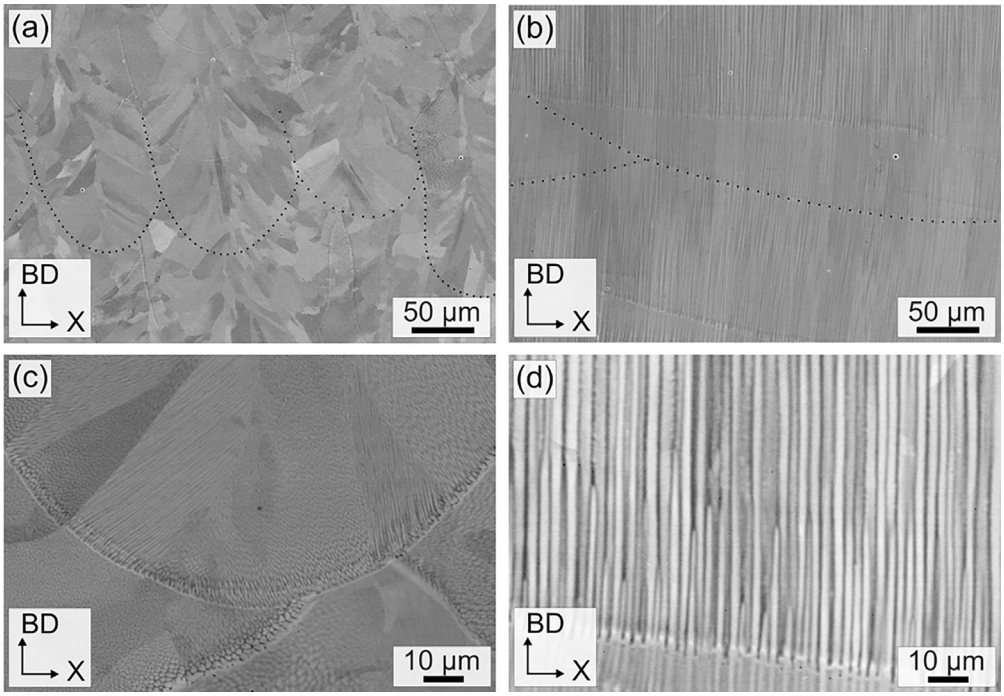

Fig. 3. SEM images (secondary electron contrast) of the X-BD plane of selected Ti-42Nb specimens LPBF-processed with a (a & c) Gaussian and (b & d) top hat laser. Dotted lines show selected melt pool boundaries.

cross sections. Having values of 0.0047 μm^{-1} (BD-X cross section) and 0.0108 μm^{-1} (X-Y cross section), the low angle boundary density is even higher than the density of the high angle boundaries.

The uniform and directional heat flow of the top hat laser supports the formation of sub grains and therefore, of low angle boundaries. Similar observations have been made by Wang and Shi [53], who reported a high fraction of low angle boundaries (misorientation: 1–15°) for an Inconel 718 sample produced with a top hat laser source.

3.2. Texture analysis

To evaluate the influence of the different laser sources on the crystallographic texture and the resulting elastic anisotropy, orientation distribution functions (ODF) were calculated from the EBSD data sets. (0 0 1), (1 1 0) and (1 1 1) pole figures as well as inverse pole figures along the testing directions of the performed tensile tests (namely X, BD and 45°; see Fig. 1) were obtained from the ODFs. To indicate the texture strength and to visualize the preferred crystal orientations for the respective specimen directions (see Fig. 5), the densities are scaled to multiples of uniform distribution (m.u.d.) so that the density value of an isotropic microstructure with a uniform distribution is 1.

The (0 0 1), (1 1 0) and (1 1 1) pole figures of the samples fabricated with a Gaussian laser show only a very weak preferred crystal orientation with density values between 0.8 and 1.5. A similar trend is shown by the inverse pole figures with only slight deviations from a uniform distribution (max. m.u.d. range: 0.6.-1.4). The Gaussian samples can, therefore, be stated as nearly crystallographic isotropic. In contrast, a very strong ⟨0 0 1⟩ fiber texture parallel to BD was achieved utilizing the top hat laser. The density of the {0 0 1} orientations is by 30-fold increased along BD and by 5–10-fold in the X-Y plane, when compared to a uniform orientation distribution. This very strong texture along BD can be explained with the nearly planar melt pool boundaries as shown in Fig. 3(b). In this case, the main thermal gradient at any side of the melt pool is vertical, which favors a vertical cell formation and grain growth towards the heat flow [53]. This can also be seen in Fig. 3(b) and (d) where the cells grow through the melt pool boundaries without altering their growth direction. A strong {0 0 1} texture development along the building direction for a top hat laser configuration was also reported by other authors for Ni-based and Fe-based alloys [53–55].

Due to the distinct relationship between the ⟨0 0 1⟩, ⟨1 1 0⟩ and ⟨1 1 1⟩ crystal directions, the strong ⟨0 0 1⟩ fiber texture along BD results in the characteristic (1 1 0) and (1 1 1) pole figures shown in Fig. 5. The density of the (1 1 0) pole figure is increased in the X-Y plane and at an angle of 45° to the X-Y plane and the density of the (1 1 1) pole figure at an angle of around 35° to the X-Y plane. These findings are also illustrated by the corresponding IPFs for X, 45° and BD.

3.3. Elastic anisotropy

For a cubic crystal structure like ß-Ti, the single crystal elastic anisotropy is given by the elastic tensor C, which is specified by the three elastic constants (C_{11}, C_{12}, C_{44}). With knowledge of C, the elastic behavior in any crystal direction can be calculated [59,62,66]. Fig. 6 shows the direction dependence of the Young's modulus of a Ti-45Nb single crystal. The calculation is based on the elastic constants (C_{11} = 137.0 GPa, C_{12} = 109.6 GPa, C_{44} = 33.17 GPa), that were experimentally determined by Hermann et al. [62] for a Ti-45Nb single crystal. The results illustrate the high elastic anisotropy of the ß-Ti crystal structure, with a maximum Young's modulus of 89.1 GPa along the ⟨1 1 1⟩ directions and a minimum Young's modulus of 41.4 GPa along the ⟨0 0 1⟩ directions. Along the ⟨1 1 0⟩ directions the Young's modulus is 67.5 GPa. Even though the absolute Young's modulus values of the Ti-42Nb alloy analyzed in this study, might slightly differ due to the lower Nb content, a representative description of the orientation dependence of the Young's modulus is still reasonable.

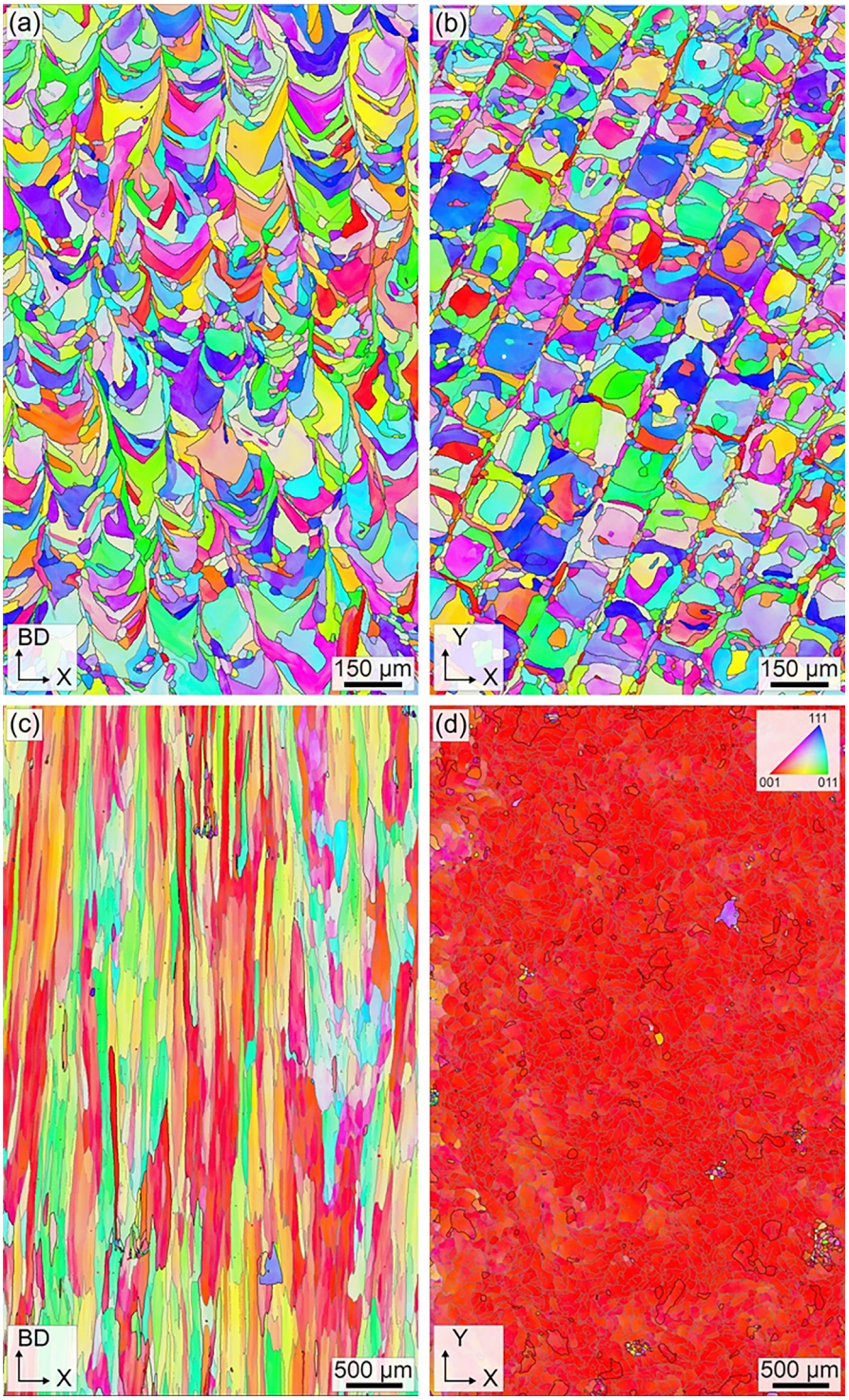

Fig. 4. Inverse pole figure (IPF) mappings of selected Ti-42Nb specimens processed with a (a, b) Gaussian and (c, d) top hat laser configuration. The IPF color coding is given with respect to the sample surface.

This strong direction dependence of the Young's modulus can be used to alter the macroscopic Young's modulus of a polycrystalline material by introducing a crystallographic texture. The macroscopic Young's modulus of such a textured polycrystal can be numerically evaluated using the elastic single crystal constants and the texture data of the polycrystal. Several studies confirm that the Hill estimation approach, which is the arithmetic average of the upper (Voigt) and lower (Reuss) bound, is capable to predict the elastic anisotropy of polycrystalline materials to a great extend [45,62,65,72]. For details about the method and the MTEX toolbox the reader is referred to Mainprice et al. [65]. For an isotropic Ti-45Nb polycrystal the macroscopic Young's modulus calculated by the Hill estimation is 65.5 GPa, which is in good accordance with experimentally determined Young's modulus values of polycrystalline Ti-45Nb (E = 62–70 GPa) [73,74].

The stereographic projections in Fig. 7a and b show the calculated direction dependence of the Young's modulus for samples fabricated with both laser types. Due to the very weak texture of

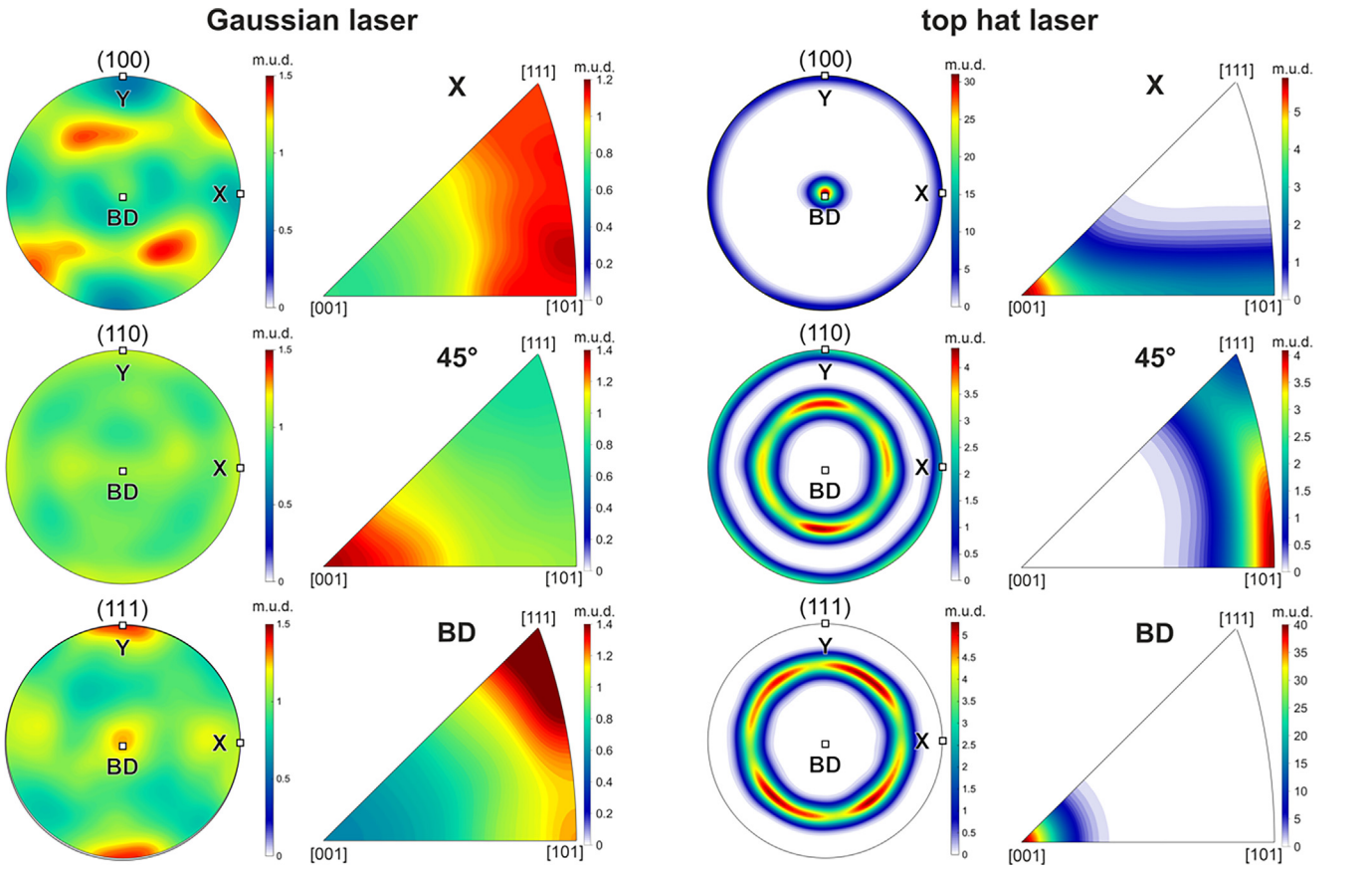

Fig. 5. Texture data of samples fabricated by LPBF with a Gaussian and a top hat laser, represented as (1 0 0), (1 1 0) and (1 1 1) pole figures and as inverse pole figures for the X direction, as well as the 45° direction and the building direction (BD).

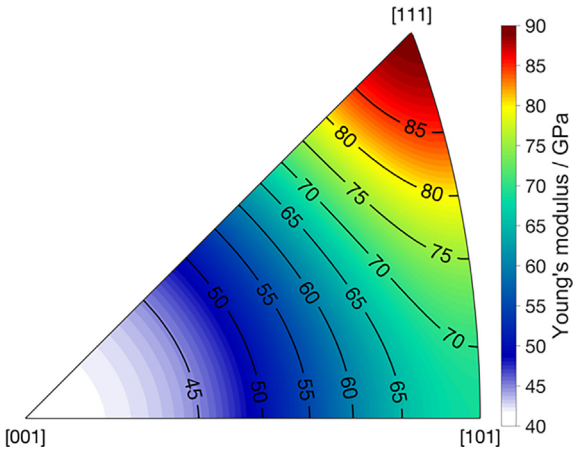

Fig. 6. Orientation dependence of the Young's modulus of a ß-type Ti-45Nb single crystal calculated after Mainprice et al. [65]. The calculation is based on the elastic single crystal constants experimentally determined by Hermann et al. [62].

the Gaussian samples only a slight variation of the Young's modulus between 62 and 68 GPa exists. For the strongly textured top hat laser sample, the model shows a significant anisotropy of the Young's modulus. A value of only 43 GPa is predicted along BD, which corresponds to a reduction of 34% compared to the value for an isotropic sample (65.5 GPa). In addition, the Young's modulus is also significantly lowered in the X-Y plane (53 GPa). A maximum Young's modulus of 78 GPa is predicted at an angle between 35° and 45° to the X-Y plane.

To verify the predicted Young's modulus values, tensile tests were performed at distinct angles of 0° (X direction), of 45°, and of 90° (BD)) relative to the X direction (in the X-BD plane). The results are shown in Fig. 7c and d together with the Hill estimation as well as the lower and the upper bound, given by the Reuss and Voigt approximation for the analyzed directions. The width of the upper and lower bound decreases with increasing texture strength and is therefore wider for the sample fabricated with the Gaussian laser. Considering the experimental errors given by the determination of the texture data and the measurement of the Young's modulus values as well as the potential difference of the elastic constants that are caused by the slight chemical deviation of the Nb content, a good agreement between the calculated and the experimentally determined Young's modulus values is evident. Nearly all experimental measurement data fit within the bounds and fall close to the Hill estimation.

For samples fabricated with a Gaussian laser, tensile tests reveal only a small difference of the Young's modulus value along the three testing directions (E_X = 69 ± 1 GPa, $E_{45°}$ = 67 ± 1 GPa, E_{BD} = 70 ± 1 GPa). Compared to the values of the Hill estimation, the experimentally determined values are slightly higher (1–3 GPa), but nevertheless confirm the nearly isotropic elastic behavior predicted by the Hill model. For the samples fabricated with the top hat laser, the experimentally determined Young's modulus values show a high anisotropy and match well with the predicted bounds. A high Young's modulus of 79 ± 3 GPa is determined at an angle of 45°, whereas a significantly lower Young's modulus of only 51 ± 2 GPa was measured along the X axis. Both values deviate around 5 GPa from the prediction made by the Hill estimation.

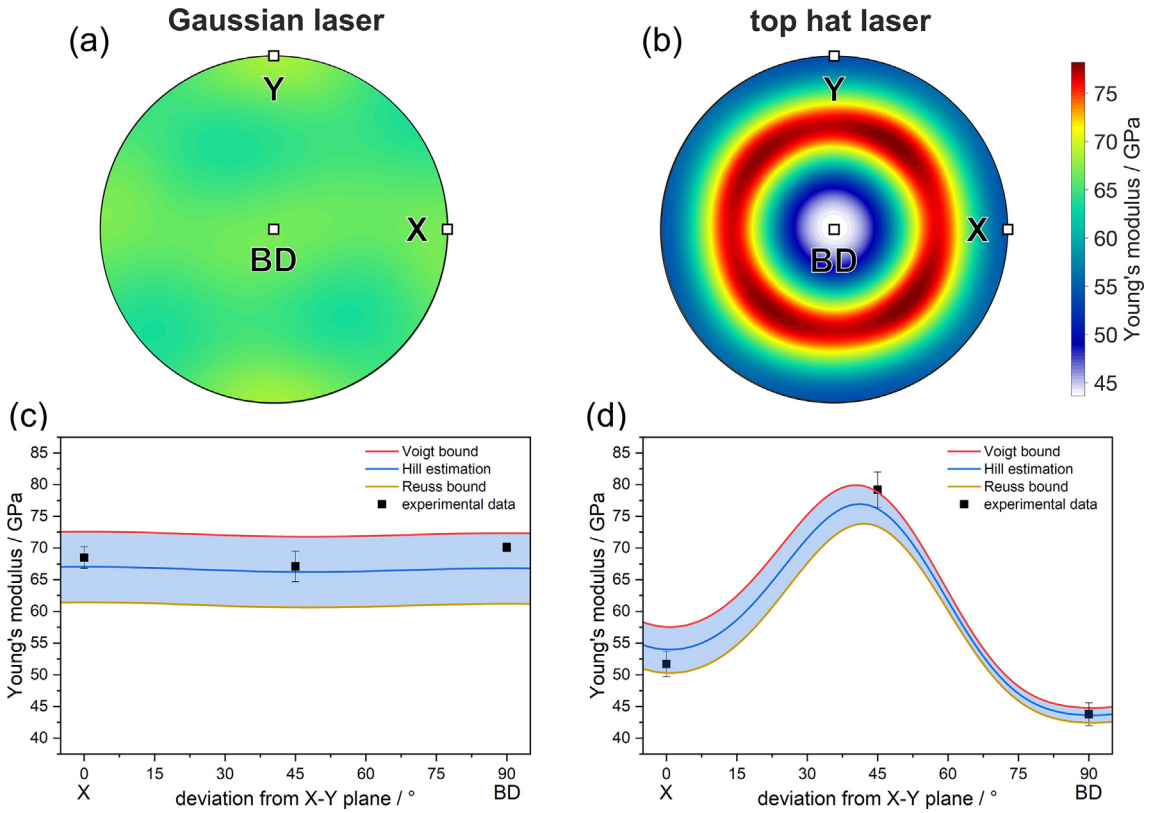

Fig. 7. Stereographic projections of the direction dependence of the Young's modulus calculated by the Hill estimation for samples processed by LPBF with a Gaussian laser and a top hat laser (a, b). Profiles of the Hill estimation and the upper (Voigt) and lower (Reuss) bounds from X to BD, together with the experimental determined Young's modulus values (c, d).

Along the BD, a Young's modulus as low as 44 ± 2 GPa was achieved. Compared to the Gaussian samples, with a nearly isotropic elastic behavior, the Young's modulus along the building direction was significantly lowered by around 36%.

3.4. Mechanical properties

From the stress-strain curves of the tensile tests (Supplementary Fig. 2) the 0.2% yield strength (0.2 %YS) and the ultimate tensile strength (UTS) values were determined for the three testing directions (X, 45° and BD). The mean values together with their standard deviation are shown in Fig. 8

Independent of the used laser source, the LPBF-processed Ti-42Nb alloy showed superior 0.2% yield strength (0.2 %YS) and ultimate tensile strength (UTS) values when compared to cast and solution-treated ß-type Ti-(40-45)Nb alloys (0.2 %YS: 315–475 MPa; UTS: 480–500 MPa) [5,75].

Samples fabricated with the Gaussian laser reached 0.2 %YS values ranging from 718 ± 4 MPa (X), to 724 ± 15 MPa (45°) and up to 742 ± 3 MPa (BD). Hereby, the maximum deviation between the different testing directions is less than 4%, representing a nearly isotropic yielding behavior. A similar trend applies for the UTS values that were determined as 732 ± 5 MPa (X), 736 ± 18 MPa (45°) and 752 ± 2 MPa (BD). The strong texture and the columnar grain morphology of the top hat laser samples lead to a much more anisotropic yielding behavior. For the 45° testing direction, the top hat laser samples reached the highest 0.2 %YS (749 ± 10 MPa) as well as the highest UTS (765 ± 17 MPa). Despite of the much larger grain size of the top hat laser samples, those values are superior to those of

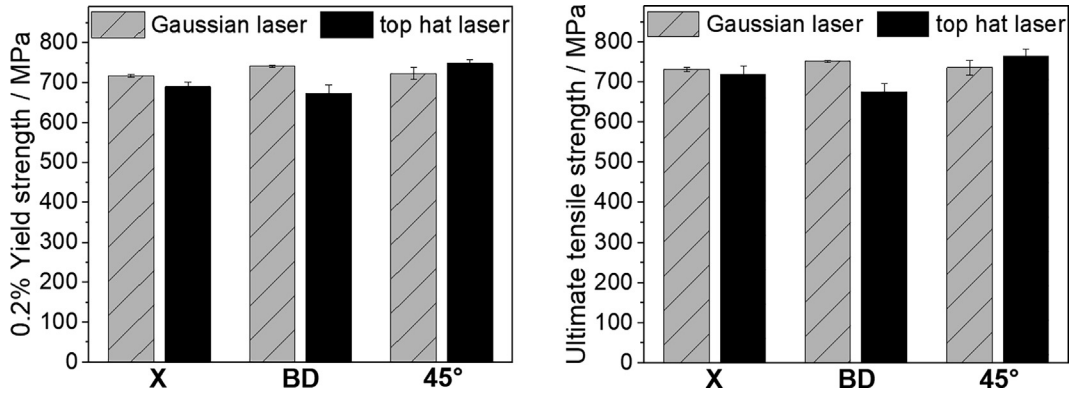

Fig. 8. Mean values of the 0.2% yield strength and the ultimate tensile strength for the loading directions X, 45° and BD of Ti-42Nb processed by LPBF with a Gaussian and a top hat laser.

the Gaussian samples. In contrast, for the X direction (0.2 %YS = 690 ± 12 MPa, UTS = 720 ± 20 MPa) and the BD (0.2 YS = 674 ± 20 MPa, UTS = 676 ± 21 MPa) significantly lower values are obtained. This equates a maximum deviation of the 0.2 %YS of around 11%. Compared to the Young's modulus, the anisotropy of the yielding behavior is therefore less pronounced. This highlights that, by utilizing a top hat laser, the Young's modulus can be significantly lowered along the building direction without lowering the yield strength in the same extend [52,66,71]. Thereby, the mechanical biofunctionality (YS/E), which is defined by the quotient of the yield strength and the Young's modulus can be increased [5]. For the Gaussian samples, depending on the testing direction, a mechanical biofunctionality of 10.48×10^{-3} up to 10.81×10^{-3} is reached. These values are higher or in the same range as the values reported by other authors for LPBF-processed ß-type Ti alloys like Ti-35Nb-7Zr-5Ta (YS/E = 3.81×10^{-3}) [34], Ti-24Nb-4Zr-8Sn (YS/E = 10.6×10^{-3}) [14] and Ti-42Nb (YS/E = 10.87×10^{-3}) [76]. By creating a highly anisotropic microstructure, utilizing the top hat laser, this value can be significantly altered for different loading directions. For the 45° direction, the mechanical biofunctionality is slightly lower (9.46×10^{-3}), but still at a high level. Parallel to the building plate (X), the biofunctionality is already increased by over 20% to 13.34×10^{-3} and along BD a value as high as 15.39×10^{-3} is reached. This represents an increase of over 40% compared to the Gaussian samples and the other discussed alloys.

4. Conclusions

With this study, we have demonstrated the influence of a Gaussian and top hat laser beam on the microstructure evolution and the mechanical properties of a novel ß-type Ti-42Nb alloy processed by LPBF. Utilizing a top hat laser configuration, a highly anisotropic microstructure with a very strong ⟨0 0 1⟩ texture parallel to the building direction and highly elongated grains (mm-range) was generated. The aforementioned microstructure results in a strong elastic anisotropy that was modeled by simulations based on the experimentally determined texture data and was confirmed by tensile test for selected loading directions. A Young's modulus as low as 44 GPa was reached parallel to the building direction. This corresponds to a reduction of over 30% compared to the values measured for the nearly isotropic Gaussian reference samples (67–69 GPa) and the ones reported in literature for LPBF-processed Ti-42Nb (e.g., 62 GPa) [76]). At the same time, a high 0.2% yield strength of 674 MPa is retained, resulting in a high mechanical biofunctionality of 15.39×10^{-3} along the building direction.

The obtained results of our study reveal the unique capability of a top hat laser configuration in LPBF to fabricate ß-type Ti-Nb parts with an adapted very low Young's modulus along the building direction. This new approach is a breakthrough towards the envisioned production of patient-specific bone implants with tailored mechanical performance for the controlled reduction of stress-shielding effects. Furthermore, we have observed an improved process stability due to the relatively large beam diameter in combination with the applied high laser power. Interestingly, this boosts the build-up rate (12.5 $mm^3/s \triangleq 45.0\ cm^3/h$), which was found to be in the range of our high-power Gaussian beam process parameters (16.5 $mm^3/s \triangleq 59.4\ cm^3/h$).

The ongoing research and first results already imply, that the build-up rate can be further increased (18.75 $mm^3/s \triangleq 67.5\ cm^3/h$) by increasing the layer thickness to 150 μm without compromising the part quality, viz. the relative density. Thus, the manufacturing time and costs of bulk implants can be significantly reduced. By applying a so-called Hull-Core-Strategy, viz. combining a Gaussian (hull: high precision and low surface roughness) as well as a top hat laser (core: adapted part properties, very high build-up rates), the fabrication of near-net-shape parts as well as sophisticated implant geometries (implementation of lattices) with different sets of parameters becomes possible. This will be presented in a subsequent work.

Funding

Funding by the Deutsche Forschungsgemeinschaft (DFG) under project GE/1106/12-1 and ZI 1006/16-1 (no 419952351) is acknowledged.

CRediT authorship contribution statement

Stefan Pilz: Conceptualization, Methodology, Investigation, Formal analysis, Visualization, Writing – original draft, Writing – review & editing. **Tobias Gustmann:** Methodology, Visualization, Writing – original draft, Writing – review & editing. **Fabian Günther:** Writing – review & editing. **Martina Zimmermann:** Writing – review & editing, Funding acquisition, Project administration. **Uta Kühn:** Writing – review & editing, Resources. **Annett Gebert:** Writing – review & editing, Funding acquisition, Project administration, Resources, Supervision.

Declaration of Competing Interest

The authors declare that they have no known competing financial interests or personal relationships that could have appeared to influence the work reported in this paper.

Acknowledgments

The authors are grateful to Heike Bußkamp and Andrea Voss for chemical analyses.

Appendix A. Supplementary material

Supplementary data to this article can be found online at https://doi.org/10.1016/j.matdes.2022.110516.

References

[1] D. Kuroda, M. Niinomi, M. Morinaga, Y. Kato, T. Yashiro, Design and mechanical properties of new β type titanium alloys for implant materials, Mater. Sci. Eng. 243 (1-2) (1998) 244–249.
[2] S.L. Sing, J. An, W.Y. Yeong, F.E. Wiria, Laser and electron-beam powder-bed additive manufacturing of metallic implants: A review on processes, materials and designs, J. Orthopaed. Res. 34 (3) (2016) 369–385, https://doi.org/10.1002/jor.23075.
[3] M. Geetha, A.K. Singh, R. Asokamani, A.K. Gogia, Ti based biomaterials, the ultimate choice for orthopaedic implants – A review, Prog. Mater. Sci. 54 (3) (2009) 397–425, https://doi.org/10.1016/j.pmatsci.2008.06.004.
[4] R. Karre, M.K. Niranjan, S.R. Dey, First principles theoretical investigations of low Young's modulus beta Ti–Nb and Ti–Nb–Zr alloys compositions for biomedical applications, Mater. Sci. Eng., C 50 (2015) 52–58, https://doi.org/10.1016/j.msec.2015.01.061.
[5] A. Helth, S. Pilz, T. Kirsten, L. Giebeler, J. Freudenberger, M. Calin, J. Eckert, A. Gebert, Effect of thermomechanical processing on the mechanical biofunctionality of a low modulus Ti-40Nb alloy, J. Mech. Behav. Biomed. 65 (2017) 137–150, https://doi.org/10.1016/j.jmbbm.2016.08.017.
[6] A. Reck, S. Pilz, M. Kuczyk, A. Gebert, M. Zimmermann, Cyclic deformation characteristics of the metastable β-type Ti–40Nb alloy, Mater. Sci. Eng. 761 (2019) 137966, https://doi.org/10.1016/j.msea.2019.05.096.
[7] S. Pilz, D. Geissler, M. Calin, J. Eckert, M. Zimmermann, J. Freudenberger, A. Gebert, Thermomechanical processing of In-containing β-type Ti-Nb alloys, J. Mech. Behav. Biomed. 79 (2018) 283–291, https://doi.org/10.1016/j.jmbbm.2017.12.028.
[8] P.F. Gostin, A. Helth, A. Voss, R. Sueptitz, M. Calin, J. Eckert, A. Gebert, Surface treatment, corrosion behavior, and apatite-forming ability of Ti-45Nb implant alloy, J. Biomed. Mater. Res. Part B Appl. Biomater. 101B (2) (2013) 269–278, https://doi.org/10.1002/jbm.b.32836.

[9] A. Gebert, S. Oswald, A. Helth, A. Voss, P.F. Gostin, M. Rohnke, J. Janek, M. Calin, J. Eckert, Effect of indium (In) on corrosion and passivity of a beta-type Ti–Nb alloy in Ringer's solution, Appl. Surf. Sci. 335 (2015) 213–222, https://doi.org/10.1016/j.apsusc.2015.02.058.
[10] A. Helth, P.F. Gostin, S. Oswald, H. Wendrock, U. Wolff, U. Hempel, S. Arnhold, M. Calin, J. Eckert, A. Gebert, Chemical nanoroughening of Ti40Nb surfaces and its effect on human mesenchymal stromal cell response, J. Biomed. Mater. Res. Part B Appl. Biomater. 102 (1) (2014) 31–41, https://doi.org/10.1002/jbm.b.32976.
[11] A. Awad, F. Fina, A. Goyanes, S. Gaisford, A.W. Basit, Advances in powder bed fusion 3D printing in drug delivery and healthcare, Adv. Drug Deliver. Rev. 174 (2021) 406–424, https://doi.org/10.1016/j.addr.2021.04.025.
[12] Y.-L. Hao, S.-J. Li, R. Yang, Biomedical titanium alloys and their additive manufacturing, Rare Met. 35 (9) (2016) 661–671, https://doi.org/10.1007/s12598-016-0793-5.
[13] J.C. Colombo-Pulgarín, C.A. Biffi, M. Vedani, D. Celentano, A. Sánchez-Egea, A.D. Boccardo, J.-P. Ponthot, Beta Titanium Alloys Processed By Laser Powder Bed Fusion: A Review, J. Mater. Eng. Perform. 30 (9) (2021) 6365–6388, https://doi.org/10.1007/s11665-021-05800-6.
[14] L.-Y. Chen, Y.-W. Cui, L.-C. Zhang, Recent Development in Beta Titanium Alloys for Biomedical Applications, Metals-Basel 10 (2020) 1139, https://doi.org/10.3390/met10091139.
[15] M. Todai, T. Nagase, T. Hori, H. Motoki, S.H. Sun, K. Hagihara, T. Nakano, Fabrication of the Beta-Titanium Alloy Rods from a Mixture of Pure Metallic Element Powders via Selected Laser Melting, Mater. Sci. Forum 941 (2018) 1260–1263.
[16] A.A. Saprykin, Y.P. Sharkeev, E.A. Ibragimov, E.V. Babakova, D.V. Dudikhin, Forming a single layer of a composite powder based on the Ti-Nb system via selective laser melting (SLM), Iop Conf. Ser. Mater. Sci. Eng. 140 (2016) 012001.
[17] M. Fischer, D. Joguet, G. Robin, L. Peltier, P. Laheurte, In situ elaboration of a binary Ti–26Nb alloy by selective laser melting of elemental titanium and niobium mixed powders, Mater. Sci. Eng., C 62 (2016) 852–859, https://doi.org/10.1016/j.msec.2016.02.033.
[18] D. Zhao, C. Han, J. Li, J. Liu, Q. Wei, In situ fabrication of a titanium-niobium alloy with tailored microstructures, enhanced mechanical properties and biocompatibility by using selective laser melting, Mater. Sci. Eng., C 111 (2020) 110784, https://doi.org/10.1016/j.msec.2020.110784.
[19] S. Dadbakhsh, M. Speirs, G. Yablokova, J.-P. Kruth, J. Schrooten, J. Luyten, et al. Microstructural Analysis and Mechanical Evaluation of Ti-45Nb Produced by Selective Laser Melting towards Biomedical Applications (2015) 421–428. https://doi.org/10.1007/978-3-319-48127-2_53..
[20] J.D. Roehling, A. Perron, J.-L. Fattebert, T. Haxhimali, G. Guss, T.T. Li, D. Bober, A. W. Stokes, A.J. Clarke, P.E.A. Turchi, M.J. Matthews, J.T. McKeown, Rapid Solidification in Bulk Ti-Nb Alloys by Single-Track Laser Melting, Jom-Us 70 (8) (2018) 1589–1597, https://doi.org/10.1007/s11837-018-2920-2.
[21] H. Schwab, K. Prashanth, L. Löber, U. Kühn, J. Eckert, Selective Laser Melting of Ti-45Nb Alloy, Metals-Basel 5 (2015) 686–694, https://doi.org/10.3390/met5020686.
[22] Y.P. Sharkeev, A.Y. Eroshenko, Z.G. Kovalevskaya, A.A. Saprykin, E.A. Ibragimov, I.A. Glukhov, M.A. Khimich, P.V. Uvarkin, E.V. Babakova, Structural and Phase State of Ti–Nb Alloy at Selective Laser Melting of the Composite Powder, Russ. Phys. J. 59 (3) (2016) 430–434, https://doi.org/10.1007/s11182-016-0790-z.
[23] S. Huang, R.L. Narayan, J.H.K. Tan, S.L. Sing, W.Y. Yeong, Resolving the porosity-unmelted inclusion dilemma during in-situ alloying of Ti34Nb via laser powder bed fusion, Acta Mater. 204 (2021) 116522, https://doi.org/10.1016/j.actamat.2020.116522.
[24] L. Zhou, T. Yuan, R. Li, J. Tang, M. Wang, F. Mei, Anisotropic mechanical behavior of biomedical Ti-13Nb-13Zr alloy manufactured by selective laser melting, J. Alloy. Compd. 762 (2018) 289–300, https://doi.org/10.1016/j.jallcom.2018.05.179.
[25] L. Zhou, T. Yuan, R. Li, J. Tang, G. Wang, K. Guo, J. Yuan, Densification, microstructure evolution and fatigue behavior of Ti-13Nb-13Zr alloy processed by selective laser melting, Powder Technol. 342 (2019) 11–23, https://doi.org/10.1016/j.powtec.2018.09.073.
[26] T. Seramak, K. Zasinska, M. Mesnard, K. Bednarz, P. Fic, A. Zielinski, Determinants of the surface quality, density and dimensional correctness in selective laser melting of the Ti-13Zr-13Nb alloy, Matériaux Techniques 106 (4) (2018) 405, https://doi.org/10.1051/mattech/2018050.
[27] L. Zhou, T. Yuan, J. Tang, J. He, R. Li, Mechanical and corrosion behavior of titanium alloys additively manufactured by selective laser melting – A comparison between nearly β titanium, α titanium and α + β titanium, Opt. Laser Technol. 119 (2019) 105625, https://doi.org/10.1016/j.optlastec.2019.105625.
[28] L. Zhou, T. Yuan, R. Li, J. Tang, M. Wang, L. Li, C. Chen, Microstructure and mechanical performance tailoring of Ti-13Nb-13Zr alloy fabricated by selective laser melting after post heat treatment, J. Alloy. Compd. 775 (2019) 1164–1176, https://doi.org/10.1016/j.jallcom.2018.10.030.
[29] L. Zhou, T. Yuan, R. Li, J. Tang, M. Wang, F. Mei, Microstructure and mechanical properties of selective laser melted biomaterial Ti-13Nb-13Zr compared to hot-forging, Mater. Sci. Eng. 725 (2018) 329–340, https://doi.org/10.1016/j.msea.2018.04.001.
[30] T. Seramak, K. Zasińska, A. Zieliński, J. Andryskowski, A. Andryskowska-Ignaczak, M. Motyl, Prosthetic Elements Made of the Ti-13Zr-13Nb Alloy by Selective Laser Melting, Adv. Mater. Res.-Switz. 17 (2017) 54–61, https://doi.org/10.1515/adms-2017-0016.
[31] L. Zhou, T. Yuan, J. Tang, L. Li, F. Mei, R. Li, Texture evolution, phase transformation and mechanical properties of selective laser melted Ti-13Nb-13Zr, Mater. Charact. 145 (2018) 185–195, https://doi.org/10.1016/j.matchar.2018.08.053.
[32] M. Speirs, J.V. Humbeeck, J. Schrooten, J. Luyten, J.P. Kruth, The Effect of Pore Geometry on the Mechanical Properties of Selective Laser Melted Ti-13Nb-13Zr Scaffolds, Proc. Cirp. 5 (2013) 79–82, https://doi.org/10.1016/j.procir.2013.01.016.
[33] L. Zhou, T. Yuan, R. Li, L. Li, Two ways of evaluating the wear property of Ti-13Nb-13Zr fabricated by selective laser melting, Mater. Lett. 242 (2019) 9–12, https://doi.org/10.1016/j.matlet.2019.01.015.
[34] R. Ummethala, P.S. Karamched, S. Rathinavelu, N. Singh, A. Aggarwal, K. Sun, E. Ivanov, L. Kollo, I. Okulov, J. Eckert, K.G. Prashanth, Selective laser melting of high-strength, low-modulus Ti–35Nb–7Zr–5Ta alloy, Materialia 14 (2020) 100941, https://doi.org/10.1016/j.mtla.2020.100941.
[35] R.L. Batalha, W.C. Batalha, L. Deng, T. Gustmann, S. Pauly, C.S. Kiminami, P. Gargarella, Processing a biocompatible Ti–35Nb–7Zr–5Ta alloy by selective laser melting, J. Mater. Res. 35 (9) (2020) 1143–1153, https://doi.org/10.1557/jmr.2020.90.
[36] L.C. Zhang, D. Klemm, J. Eckert, Y.L. Hao, T.B. Sercombe, Manufacture by selective laser melting and mechanical behavior of a biomedical Ti–24Nb–4Zr–8Sn alloy, Scr. Mater. 65 (1) (2011) 21–24, https://doi.org/10.1016/j.scriptamat.2011.03.024.
[37] Y.J. Liu, S.J. Li, H.L. Wang, W.T. Hou, Y.L. Hao, R. Yang, T.B. Sercombe, L.C. Zhang, Microstructure, defects and mechanical behavior of beta-type titanium porous structures manufactured by electron beam melting and selective laser melting, Acta Mater. 113 (2016) 56–67, https://doi.org/10.1016/j.actamat.2016.04.029.
[38] Y.J. Liu, X.P. Li, L.C. Zhang, T.B. Sercombe, Processing and properties of topologically optimised biomedical Ti–24Nb–4Zr–8Sn scaffolds manufactured by selective laser melting, Mater. Sci. Eng. 642 (2015) 268–278, https://doi.org/10.1016/j.msea.2015.06.088.
[39] L.C. Zhang, T.B. Sercombe, Selective Laser Melting of Low-Modulus Biomedical Ti-24Nb-4Zr-8Sn Alloy: Effect of Laser Point Distance, Key Eng. Mat. 520 (2012) 226–233, https://doi.org/10.4028/www.scientific.net/kem.520.226.
[40] C.L. Yang, Z.J. Zhang, S.J. Li, Y.J. Liu, T.B. Sercombe, W.T. Hou, P. Zhang, Y.K. Zhu, Y.L. Hao, Z.F. Zhang, R. Yang, Simultaneous improvement in strength and plasticity of Ti-24Nb-4Zr-8Sn manufactured by selective laser melting, Mater. Design 157 (2018) 52–59, https://doi.org/10.1016/j.matdes.2018.07.036.
[41] S. Pauly, P. Wang, U. Kühn, K. Kosiba, Experimental determination of cooling rates in selectively laser-melted eutectic Al-33Cu, Addit. Manuf. 22 (2018) 753–757, https://doi.org/10.1016/j.addma.2018.05.034.
[42] T. Ishimoto, K. Hagihara, K. Hisamoto, S.-H. Sun, T. Nakano, Crystallographic texture control of beta-type Ti–15Mo–5Zr–3Al alloy by selective laser melting for the development of novel implants with a biocompatible low Young's modulus, Scr. Mater. 132 (2017) 34–38, https://doi.org/10.1016/j.scriptamat.2016.12.038.
[43] T. Nagase, T. Hori, M. Todai, S.-H. Sun, T. Nakano, Additive manufacturing of dense components in beta–titanium alloys with crystallographic texture from a mixture of pure metallic element powders, Mater. Design 173 (2019) 107771, https://doi.org/10.1016/j.matdes.2019.107771.
[44] J.J. Marattukalam, D. Karlsson, V. Pacheco, P. Beran, U. Wiklund, U. Jansson, B. Hjörvarsson, M. Sahlberg, The effect of laser scanning strategies on texture, mechanical properties, and site-specific grain orientation in selective laser melted 316L SS, Mater. Design 193 (2020) 108852, https://doi.org/10.1016/j.matdes.2020.108852.
[45] F. Geiger, K. Kunze, T. Etter, Tailoring the texture of IN738LC processed by selective laser melting (SLM) by specific scanning strategies, Mater. Sci. Eng. 661 (2016) 240–246, https://doi.org/10.1016/j.msea.2016.03.036.
[46] E. Hamed, I. Jasiuk, Elastic modeling of bone at nanostructural level, Mater. Sci. Eng. R Rep. 73 (3-4) (2012) 27–49, https://doi.org/10.1016/j.mser.2012.04.001.
[47] S. Hanada, N. Masahashi, T.-K. Jung, N. Yamada, G. Yamako, E. Itoi, Fabrication of a high-performance hip prosthetic stem using β Ti–33.6Nb–4Sn, J. Mech. Behav. Biomed. 30 (2014) 140–149, https://doi.org/10.1016/j.jmbbm.2013.11.002.
[48] M.C. Sow, T. De Terris, O. Castelnau, Z. Hamouche, F. Coste, R. Fabbro, P. Peyre, Influence of beam diameter on Laser Powder Bed Fusion (L-PBF) process, Addit. Manuf. 36 (2020) 101532, https://doi.org/10.1016/j.addma.2020.101532.
[49] A. Okunkova, M. Volosova, P. Peretyagin, Y. Vladimirov, I. Zhirnov, A.V. Gusarov, Experimental Approbation of Selective Laser Melting of Powders by the Use of Non-Gaussian Power Density Distributions, Phys. Proc. 56 (2014) 48–57, https://doi.org/10.1016/j.phpro.2014.08.095.
[50] A.S. Metel, M.M. Stebulyanin, S.V. Fedorov, A.A. Okunkova, Power Density Distribution for Laser Additive Manufacturing (SLM): Potential, Fundam. Adv. Appl. Technol. 7 (2018) 5, https://doi.org/10.3390/technologies7010005.
[51] M.L. Montero-Sistiaga, M. Godino-Martinez, K. Boschmans, J.-P. Kruth, J.V. Humbeeck, K. Vanmeensel, Microstructure evolution of 316L produced by HP-SLM (high power selective laser melting), Addit. Manuf. 23 (2018) 402–410, https://doi.org/10.1016/j.addma.2018.08.028.
[52] M.L. Montero-Sistiaga, S. Pourbabak, J. Van Humbeeck, D. Schryvers, K. Vanmeensel, Microstructure and mechanical properties of Hastelloy X produced by HP-SLM (high power selective laser melting), Mater. Design 165 (2019) 107598, https://doi.org/10.1016/j.matdes.2019.107598.
[53] Y. Wang, J. Shi, Developing very strong texture in a nickel-based superalloy by selective laser melting with an ultra-high power and flat-top laser beam, Mater. Charact. 165 (2020) 110372, https://doi.org/10.1016/j.matchar.2020.110372.

[54] V.A. Popovich, E.V. Borisov, A.A. Popovich, V.S. Sufiiarov, D.V. Masaylo, L. Alzina, Functionally graded Inconel 718 processed by additive manufacturing: Crystallographic texture, anisotropy of microstructure and mechanical properties, Mater. Design 114 (2017) 441–449, https://doi.org/10.1016/j.matdes.2016.10.075.
[55] T. Niendorf, S. Leuders, A. Riemer, H.A. Richard, T. Tröster, D. Schwarze, Highly Anisotropic Steel Processed by Selective Laser Melting, Metall. Mater. Trans. B 44 (4) (2013) 794–796, https://doi.org/10.1007/s11663-013-9875-z.
[56] M. Yonehara, T.-T. Ikeshoji, T. Nagahama, T. Mizoguchi, M. Tano, T. Yoshimi, H. Kyogoku, Parameter optimization of the high-power laser powder bed fusion process for H13 tool steel, Int. J. Adv. Manuf. Technol. 110 (1-2) (2020) 427–437, https://doi.org/10.1007/s00170-020-05879-6.
[57] L.E. Loh, Z.H. Liu, D.Q. Zhang, M. Mapar, S.L. Sing, C.K. Chua, W.Y. Yeong, Selective Laser Melting of aluminium alloy using a uniform beam profile, Virtual Phys. Prototyp. 9 (1) (2014) 11–16, https://doi.org/10.1080/17452759.2013.869608.
[58] D. Buchbinder, H. Schleifenbaum, S. Heidrich, W. Meiners, J. Bültmann, High Power Selective Laser Melting (HP SLM) of Aluminum Parts, Phys. Proc. 12 (2011) 271–278, https://doi.org/10.1016/j.phpro.2011.03.035.
[59] M. Tane, S. Akita, T. Nakano, K. Hagihara, Y. Umakoshi, M. Niinomi, H. Nakajima, Peculiar elastic behavior of Ti–Nb–Ta–Zr single crystals, Acta Mater. 56 (12) (2008) 2856–2863, https://doi.org/10.1016/j.actamat.2008.02.017.
[60] M. Tane, S. Akita, T. Nakano, K. Hagihara, Y. Umakoshi, M. Niinomi, H. Mori, H. Nakajima, Low Young's modulus of Ti–Nb–Ta–Zr alloys caused by softening in shear moduli c′ and c44 near lower limit of body-centered cubic phase stability, Acta Mater. 58 (20) (2010) 6790–6798, https://doi.org/10.1016/j.actamat.2010.09.007.
[61] S.-H. Lee, M. Todai, M. Tane, K. Hagihara, H. Nakajima, T. Nakano, Biocompatible low Young's modulus achieved by strong crystallographic elastic anisotropy in Ti–15Mo–5Zr–3Al alloy single crystal, J. Mech. Behav. Biomed. 14 (2012) 48–54, https://doi.org/10.1016/j.jmbbm.2012.05.005.
[62] R. Hermann, H. Hermann, M. Calin, B. Büchner, J. Eckert, Elastic constants of single crystalline β-Ti70Nb30, Scr. Mater. 66 (3-4) (2012) 198–201, https://doi.org/10.1016/j.scriptamat.2011.10.039.
[63] K. Hagihara, T. Nakano, H. Maki, Y. Umakoshi, M. Niinomi, Isotropic plasticity of β-type Ti-29Nb-13Ta-4.6Zr alloy single crystals for the development of single crystalline β-Ti implants, Sci. Rep.-Uk 6 (1) (2016), https://doi.org/10.1038/srep29779.
[64] AMtrinsic® Spherical Ti-42Nb Powder, n.d. https://www.taniobis.com/home/products/productinformations/amtrinsic-spherical-ti-42nb-powder~cc.en.html (accessed June 8, 2021)..
[65] D. Mainprice, R. Hielscher, H. Schaeben, Calculating anisotropic physical properties from texture data using the MTEX open-source package, Geol. Soc. Lond. Special Publ. 360 (1) (2011) 175–192.
[66] D. Mainprice, F. Bachmann, R. Hielscher, H. Schaeben, G.E. Lloyd, Calculating anisotropic piezoelectric properties from texture data using the MTEX open source package, Geol. Soc. Lond. Special Publ. 409 (2015) 223–249, https://doi.org/10.1144/sp409.2.
[67] C. Tenbrock, F.G. Fischer, K. Wissenbach, J.H. Schleifenbaum, P. Wagenblast, W. Meiners, J. Wagner, Influence of keyhole and conduction mode melting for top-hat shaped beam profiles in laser powder bed fusion, J. Mater. Process. Tech. 278 (2020) 116514, https://doi.org/10.1016/j.jmatprotec.2019.116514.
[68] H. Schwab, M. Bönisch, L. Giebeler, T. Gustmann, J. Eckert, U. Kühn, Processing of Ti-5553 with improved mechanical properties via an in-situ heat treatment combining selective laser melting and substrate plate heating, Mater. Design 130 (2017) 83–89, https://doi.org/10.1016/j.matdes.2017.05.010.
[69] L. Thijs, K. Kempen, J.-P. Kruth, J. Van Humbeeck, Fine-structured aluminium products with controllable texture by selective laser melting of pre-alloyed AlSi10Mg powder, Acta Mater. 61 (5) (2013) 1809–1819, https://doi.org/10.1016/j.actamat.2012.11.052.
[70] J. Liu, G. Li, Q. Sun, H.u. Li, J. Sun, X. Wang, Understanding the effect of scanning strategies on the microstructure and crystallographic texture of Ti-6Al-4V alloy manufactured by laser powder bed fusion, J. Mater. Process Tech. 299 (2022) 117366, https://doi.org/10.1016/j.jmatprotec.2021.117366.
[71] O. Gokcekaya, T. Ishimoto, S. Hibino, J. Yasutomi, T. Narushima, T. Nakano, Unique crystallographic texture formation in Inconel 718 by laser powder bed fusion and its effect on mechanical anisotropy, Acta Mater. 212 (2021) 116876, https://doi.org/10.1016/j.actamat.2021.116876.
[72] A. Charmi, R. Falkenberg, L. Ávila, G. Mohr, K. Sommer, A. Ulbricht, M. Sprengel, R. Saliwan Neumann, B. Skrotzki, A. Evans, Mechanical anisotropy of additively manufactured stainless steel 316L: An experimental and numerical study, Mater. Sci. Eng. 799 (2021) 140154, https://doi.org/10.1016/j.msea.2020.140154.
[73] S. Hanada, H. Matsumoto, S. Watanabe, Mechanical compatibility of titanium implants in hard tissues, Int. Congr. Ser. 1284 (2005) 239–247, https://doi.org/10.1016/j.ics.2005.06.084.
[74] R. Schmidt, S. Pilz, I. Lindemann, C. Damm, J. Hufenbach, A. Helth, D. Geissler, A. Henss, M. Rohnke, M. Calin, M. Zimmermann, J. Eckert, M.H. Lee, A. Gebert, Powder metallurgical processing of low modulus β-type Ti-45Nb to bulk and macro-porous compacts, Powder Technol. 322 (2017) 393–401, https://doi.org/10.1016/j.powtec.2017.09.015.
[75] A. Reck, S. Pilz, U. Thormann, V. Alt, A. Gebert, M. Calin, C. Heiß, M. Zimmermann, G. Hénaff, Effects of thermomechanical history and environment on the fatigue behavior of (β)-Ti-Nb implant alloys, Matec Web Conf 165 (2018) 06001, https://doi.org/10.1051/matecconf/201816506001.
[76] C. Schulze, M. Weinmann, C. Schweigel, O. Keßler, R. Bader, Mechanical Properties of a Newly Additive Manufactured Implant Material Based on Ti-42Nb, Materials 11 (2018) 124, https://doi.org/10.3390/ma11010124.